RSC Advances

ROYAL SOCIETY
OF **CHEMISTRY**

www.rsc.org/advances

RSC Advances

ARTICLE

Enhancement of the Oxygen Evolution Reaction in Mn^{3+}-based Electrocatalysts: Correlation between Jahn-Teller Distortion and Catalytic Activity

Shigeto Hirai,[*a] Yagi Shunsuke,[b] Akihiro Seno,[c] Masaya Fujioka,[c] Tomoya Ohno[a] and Takeshi Matsuda[a]

We systematically studied the catalytic activity of the oxygen evolution reaction (OER) for the tetragonal spinel oxide Mn$_{3-x}$Co$_x$O$_4$ ($0 \leq x < 1$ and $1 < x \leq 1.5$). The OER catalytic activity of Mn$_{3-x}$Co$_x$O$_4$ ($0 \leq x < 1$) dramatically improved with an increase in Co content. We found that the OER activity of Mn$_{3-x}$Co$_x$O$_4$ ($0 \leq x < 1$) increased linearly with the suppression of the Jahn-Teller distortion. We therefore propose that the Jahn-Teller distortion plays an important role in the OER activities of compounds containing Mn^{3+}. Mn$_{3-x}$Co$_x$O$_4$ ($0 \leq x < 1$) provides a rare case for directly studying the effect of the Jahn-Teller distortion on OER activity.

1 Introduction

The material design of low cost and highly active catalysts for energy storage applications is crucial for solving global energy problems. The oxygen evolution reaction (OER) is used for charging rechargeable metal-air batteries[1,2] and in direct solar water splitting.[3,4] Although precious metal-based catalysts with high OER activities (such as RuO$_2$ and IrO$_2$[5]) facilitate the reaction, the kinetics of the OER are rather sluggish due to its multistep proton coupled electron transfer.[4] It is therefore important to explore the mechanism of the OER and to discover and develop a highly active catalyst for the process.

As demonstrated by Suntivich et al.,[6] when the number of electrons in the e$_g$ orbital is close to unity for transition metals, perovskite oxides exhibit maximum OER activity. In other words, Mn^{3+} (t$_{2g}^3$ e$_g^1$ for both surface and bulk), Co^{3+} (t$_{2g}^5$ e$_g^1$ for surface), and Ni^{3+} (t$_{2g}^6$ e$_g^1$ for both surface and bulk) are OER active sites for Mn^{3+}, Co^{3+}, and Ni^{3+}-based perovskite oxides.[6,7,8,9] However, LaMnO$_3$ exhibits a significantly lower specific OER activity compared with LaCoO$_3$ and LaNiO$_3$ (~6% of LaNiO$_3$ at 1.8 V vs. RHE).[10] It is therefore important to explore what causes degradation of the OER activity of Mn^{3+}-based (t$_{2g}^3$ e$_g^1$) compounds to improve their catalytic activity. Among such compounds, Mn$_3$O$_4$ (Mn^{2+}[Mn^{3+}]$_2$O$_4$) is abundant in nature as the mineral hausmannite,[11] and is an inexpensive and effective catalyst for limiting the emission of carbon monoxide and NO$_x$.[12,13] Mn$_3$O$_4$ adopts a tetragonally distorted spinel structure (Fig. 1) under ambient conditions[14,15] due to the Jahn-Teller active Mn^{3+} (t$_{2g}^3$ e$_g^1$) occupying the octahedral site. The Jahn-Teller distorted Mn^{3+}O$_6$ octahedra consist of four

shorter Mn-O bonds (0.192 nm) and two longer Mn-O bonds (0.228 nm).[15] Although Mn$_3$O$_4$ contains the OER active site (i.e. Mn^{3+}) previous studies report a low specific OER activity (~40% of Mn$_2$O$_3$ at 1.8 V vs. RHE[16]) similar to LaMnO$_3$.
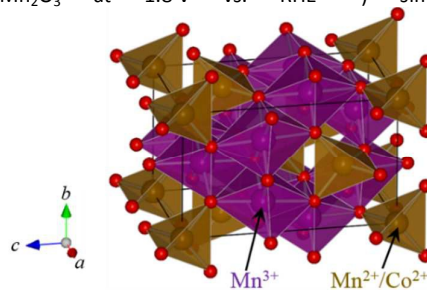

Fig. 1 Schematic image of the crystal structure of Mn$_{3-x}$Co$_x$O$_4$ nanoparticles.

We herein attempt to improve the performance of Mn$_3$O$_4$ by controlling the degradation of its OER activity. To directly compare the OER activities of Mn^{3+}-based spinel oxides, Mn^{3+} concentrations at the octahedral site and at the tetragonally distorted structure must be maintained. Mn$_{3-x}$Co$_x$O$_4$ ($0 \leq x < 1$), a series of tetragonally distorted spinel compounds, provide such an opportunity, as their octahedral sites remain occupied by only Mn^{3+} ions.[17,18] Although the OER activities of Mn$_2$CoO$_4$[19,20] (usually tetragonal phase) and Mn$_y$Co$_{3-y}$O$_4$ ($0 \leq y \leq 1$)[19,21,22] (usually cubic phase) have been previously studied, the OER activities of Mn$_{3-x}$Co$_x$O$_4$ ($0 \leq x < 1$) have not been studied. We therefore chose to systematically study the OER performance of tetragonal Mn$_{3-x}$Co$_x$O$_4$ ($0 \leq x < 1$ and $1 < x \leq 1.5$). Nanoparticles were prepared at ~20 °C to minimize the influence of geometric factors (e.g., morphology and surface area) and to minimize the influence of the statistical error for catalytic activity per unit mass.

2 Experimental

2.1 Preparation and Characterization

Mn$_{3-x}$Co$_x$O$_4$ ($0 \leq x \leq 1.5$) nanoparticles were synthesized at room temperature according to the following liquid phase synthetic

a. *Department of Materials Science and Engineering, Kitami Institute of Technology, 165 Koen-cho, Kitami 090-8507, Japan. Email: hirai@mail.kitami-it.ac.jp*

b. *Nanoscience and Nanotechnology Research Center, Osaka Prefecture University, Osaka 599-8570, Japan*

c. *Laboratory of Nano-Structure Physics, Research Institute for Electronic Science, Hokkaido University, Sapporo 001-0021, Japan*

RSC Advances Accepted Manuscript

process. $Mn(CH_3COO)_2 \cdot 4H_2O$ (Wako, 99.9%) and $Co(CH_3COO)_2 \cdot 4H_2O$ (Wako, 99.9%) (total 2 mmol) in a stoichiometric molar ratio were dissolved in a mixture of ethanol (17 mL) and distilled water (5 mL). The solution was mixed in air for 10 min at ~20 °C to give a homogenous solution. $NH_3 \cdot H_2O$ (9 mL, Wako, 25-28 wt.%) was then added, and mixed under air for 20 min at ~20 °C to evenly disperse the particles in the solution. The resulting mixture was centrifuged for 15 min at 8000 rpm, and the supernatant removed. The obtained wet product was washed twice with excess ethanol, and dried at 70 °C for 24 h to remove any residual ethanol and water.

The prepared $Mn_{3-x}Co_xO_4$ (0 ≤ x ≤ 1.5) nanoparticles were investigated by powder X-ray diffraction (XRD) using a Rigaku SmartLab diffractometer with Cu Kα radiation (λ= 1.5418 Å, 45 kV, 200 mA, step size = 0.02 °/s). GSAS software was used for Rietveld refinement of the crystal structure.[23] The value of x in the $Mn_{3-x}Co_xO_4$ nanoparticles were determined on the basis of lattice constants, specifically the Jahn-Teller distortion indicator: $c/\sqrt{2}a$ which decreases with the increase of the Co content. First, the values of x were calculated using the initial molar ratio in the starting material. Then, the validity of x in the nanoparticles was checked by comparing the values of $c/\sqrt{2}a$ in this study with those obtained by neutron diffraction studies in Bordeneuve et al.[17] (Fig. S3(d)).

Transmission electron microscopy (TEM) was conducted on selected nanoparticle samples (x = 0, 0.3, 0.6, 0.9) using an H-9000 NAR (Hitachi Ltd.) with an acceleration voltage of 300 kV. Nitrogen Brunauer–Emmett–Teller (BET) surface area measurements were conducted for the $Mn_{3-x}Co_xO_4$ (0 ≤ x ≤ 0.9) nanoparticles at 77 K with a conventional high vacuum static system.

**2.2 Electrochemical measurement of the OER activity**

The catalyst inks of the nanoparticle samples for electrochemical measurement were prepared referring to the methods reported by Suntivich et al.[6,24] and Jung et al.[25] K^+ ion-exchanged Nafion® was used as an immobilizing binder, enabling smooth transport of dissolved O_2 to the surface of the catalysts. A 3.33 wt% K^+ ion-exchanged Nafion® suspension was first obtained from a mixture of 5 wt% proton-type Nafion® suspension (Sigma-Aldrich) and a 0.1 M aqueous KOH solution in a 2:1 (*v/v*) ratio. This process increased the pH of the initial 5 wt% proton-type Nafion® suspension from 1-2 to 11. The catalyst inks of $Mn_{3-x}Co_xO_4$ (0 ≤ x ≤ 1.5) nanoparticle samples were prepared from a mixture of the as-prepared samples (25 mg), acetylene black (AB, Denka, 5 mg), and 3.33 wt% K^+ ion-exchanged Nafion® suspension (1.5 mL). The total ink volumes were adjusted to 5 mL by the addition of tetrahydrofuran (THF, Sigma Aldrich), to give final concentrations of 5 mg sample/mL, 1 mg AB/mL, and 10 mg Nafion/mL in the ink. A sample of the ink (6.4 µL) was then drop-casted on a rotating ring-disk electrode composed of a glassy carbon (GC) disk (0.2 × 0.2 × π cm^2) (BAS Inc., Japan) and a Pt ring (ϕ_{inner} = 0.5 cm, ϕ_{outer} = 0.7 cm) (BAS Inc., Japan), which was used as the working electrode after mirror polishing with 0.05 µg alumina slurry (BAS Inc., Japan). The rotating ring-disk electrode bearing the $Mn_{3-x}Co_xO_4$ (0 ≤ x ≤ 1.5) ink was then dried overnight under vacuum at room temperature.

Electrochemical measurements were conducted using a rotating ring disk electrode rotator (RRDE-3A, BAS Inc., Japan) at 1600 rpm, in combination with a bipotentiostat (ALS Co., Ltd, Japan). In addition, a Pt wire counter electrode, and an Hg/HgO reference electrode (International Chemistry Co., Ltd., Japan) filled with 0.10 M KOH (Nacalai Tesque, Inc., Japan) were used. Electrochemical measurements were conducted with O_2 saturation (30 min bubbling O_2 gas through the solution) at ~25 °C, where the

equilibrium potential of the O_2/H_2O redox couple was fixed at 0.304 V vs. Hg/HgO (or 1.23 V vs. RHE). During OER current density measurements (100 cycles for x = 0, 0.3, 0.6, 0.9, 1.5, and 10 cycles for x = 1.2) for each $Mn_{3-x}Co_xO_4$ (0 ≤ x ≤ 1.5) sample, the potential of the sample-modified GC was controlled from 0.3-0.9 V vs. Hg/HgO (1.226-1.826 V vs. RHE) at 10 mV/s. For all measurements, the OER current density was *iR*-corrected (R = ~43 Ω) using the measured solution resistance, and capacitance-corrected by averaging the anodic and cathodic scans[6] to remove the influence of the current related to the formation of an electrical double layer. For comparison, specific OER activities, Tafel slopes,[26,27] and overpotentials of the $Mn_{3-x}Co_xO_4$ (0 ≤ x ≤ 1.5) samples were obtained from the OER current density data (up to 100 cycles).

3 Results and discussion

XRD patterns (Fig. S1) demonstrate that the prepared $Mn_{3-x}Co_xO_4$ (x = 0, 0.3, 0.6, 0.9, 1.2, 1.5) samples are single-phase. All XRD peaks were indexed by the distorted spinel structure with the tetragonal space group $I4_1/amd$. The morphologies of the $Mn_{3-x}Co_xO_4$ (x = 0, 0.3, 0.6, 0.9) samples were then examined by TEM (Fig. 2). As shown in Fig. 2, the TEM images show nanoparticles with an isotropic morphology, exhibiting average particle sizes of ~17 nm for x = 0 and ~15 nm for x = 0.3-0.9.
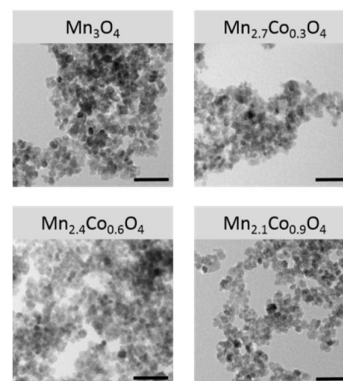

Fig. 2 Typical transmission electron microscopy (TEM) images of $Mn_{3-x}Co_xO_4$ nanoparticles for x = 0, 0.3, 0.6, and 0.9. All scale bars equal 100 nm.

In terms of site occupancy, the tetragonally distorted $Mn_{3-x}Co_xO_4$ spinel (x = 0, 0.3, 0.6, 0.9, 1.2, 1.5) can be divided into two groups, i.e. 0 ≤ x < 1 and 1 < x ≤ 1.5. The octahedral site of the former group is occupied only by the Mn^{3+} ions (Fig. S2(a))[17], while the octahedral site of the latter group is composed of a mixture of Mn^{3+}, Co^{3+}, Mn^{4+}, and Co^{2+} ions[17]. To determine the key factor that determines the OER catalytic performance of the $Mn_{3-x}Co_xO_4$ spinel materials, we first chose to focus on the $Mn_{3-x}Co_xO_4$ (0 ≤ x < 1) group.

Fig. 3(a) shows the capacitance-corrected voltammetry curves of the oxygen evolution reaction (OER) for $Mn_{3-x}Co_xO_4$ (0 ≤ x <1). The higher the OER current density is, the higher the OER activity of the catalyst is. Therefore, Fig. 3(a) demonstrates that the OER activity of $Mn_{3-x}Co_xO_4$ (0 ≤ x <1) elevates with the increase in Co content. Fig. 3(b) shows the linear correlation between the logarithmic OER current density and the *iR*-corrected potential for $Mn_{3-x}Co_xO_4$ (0 ≤ x <1), known as the Tafel plot[26,27]. The data used in Fig. 3(b) were extracted from Fig. 3(a). The smaller the slope of the Tafel plot (called Tafel slope) is, the higher the OER activity of the catalyst is. Fig. 3(b) exhibits the elevation of the OER activity with the increase

in Co content. Fig. 3(c) shows the correlation between the OER current density at 1.76 V vs. RHE (specific OER activity) and the Jahn-Teller distortion indicator: $c/\sqrt{2}a$. Specific OER activities were compared at 1.76 V vs. RHE to minimize the influence of the statistical error. Fig. 3(d) shows the durability of $Mn_{3-x}Co_xO_4$ ($0 \leq x < 1$) as OER catalysts. Evaluation of durability is important when putting catalysts into application for metal-air batteries. The ratio of Tafel slope of cycle 100 towards cycle 1 was used as an indicator of the durability. Longer term stability as an OER catalyst was observed for Co-enriched members (Fig. 3(d)). All these figures (Fig. 3) demonstrate that the OER performance of $Mn_{3-x}Co_xO_4$ ($0 \leq x < 1$) improves with the increase in Co content. In particular, $Mn_{2.1}Co_{0.9}O_4$ exhibited an excellent OER performance with a high specific OER activity (1700 % of Mn_3O_4 at 1.76 V vs. RHE), along with long-term stability over 100 cycles (>3.3 h). As recently reported for perovskite oxides,[6,7,8,9] when the number of electrons in the e_g orbital is close to unity for transition metal ions, they play the role of OER active sites. In the case of $Mn_{3-x}Co_xO_4$ ($0 \leq x < 1$), Mn^{3+} ($t_{2g}^3 e_g^1$) at the octahedral site forms an antibonding e_g orbital with the oxygen-related adsorbates (O_2^{2-} and O^{2-}). The antibonding Mn^{3+} e_g orbital has the strongest overlap with oxygen since it is at a higher energy level relative to the bonding t_{2g} orbitals of Mn^{3+} and the antibonding t_{2g} orbitals of $Mn^{2+}(e_g^2 t_{2g}^3)/Co^{2+}(e_g^4 t_{2g}^3)$ at the tetrahedral site (Fig. 4). Therefore, Mn^{3+} becomes the OER active site for $Mn_{3-x}Co_xO_4$ ($0 \leq x < 1$). Since the number of Mn^{3+} e_g electrons remained constant with an increase in Co content (only Mn^{3+} ions occupied the octahedral site), the higher OER activities of Co-enriched members could not be explained by the number of e_g electrons. In addition, as the surface areas of $Mn_{3-x}Co_xO_4$ ($x = 0.3$, 0.6, 0.9) are ~1.2 times that of Mn_3O_4,[28] this small variation of surface area cannot be used to explain the different OER activities for $Mn_{3-x}Co_xO_4$ ($0 \leq x < 1$). Furthermore, the influence of electrical conductivity can be neglected as it remains almost constant for $0 \leq x < 1$ (Fig. S2(b)). Thus, it is necessary to find alternative explanations for the higher OER activities of the Co-enriched species.
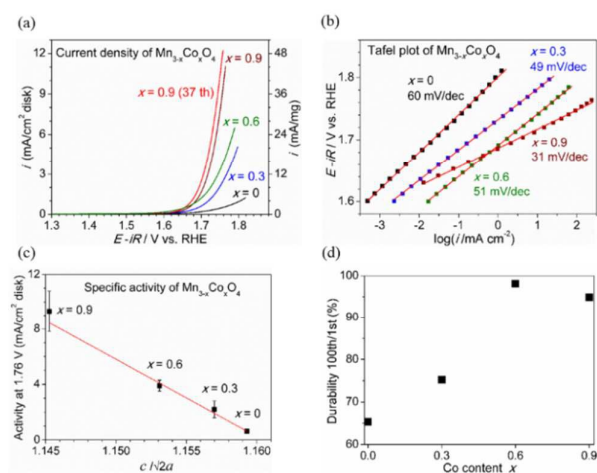
Fig. 3 (a) Linear sweep voltammetry curves of the OER (cycle 10) for $Mn_{3-x}Co_xO_4$ ($x = 0, 0.3, 0.6, 0.9$) in 0.10 M aqueous KOH at 10 mV/s. (b) Tafel plots and the variation of Tafel slopes (cycle 10) for $Mn_{3-x}Co_xO_4$ ($x = 0, 0.3, 0.6, 0.9$). (c) Variation of the specific OER activities (cycles 1-10) for $Mn_{3-x}Co_xO_4$ ($x = 0, 0.3, 0.6, 0.9$) towards the Jahn-Teller distortion indicator: $c/\sqrt{2}a$. (d) The OER durability of $Mn_{3-x}Co_xO_4$ ($x = 0, 0.3, 0.6, 0.9$). The ratio of the Tafel slope

of cycle 100 towards cycle 1 (%) was used as an indicator of the OER durability.
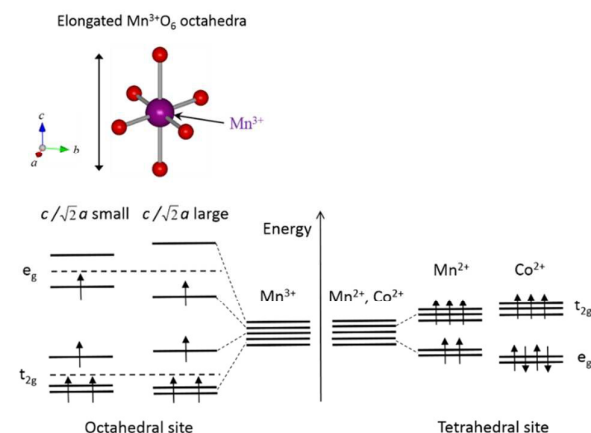
Fig. 4 Schematic view of the Mn^{3+} $3d$ orbital energy levels at the octahedral site and the Mn^{2+}/Co^{2+} $3d$ orbitals at the tetrahedral site for $Mn_{3-x}Co_xO_4$ ($0 \leq x < 1$). Triply degenerated Mn^{3+} t_{2g} orbitals and doubly degenerated Mn^{3+} e_g orbitals split into two energy levels to lower the total energy of the Mn^{3+} $3d$ electrons (Jahn-Teller effect). The $Mn^{3+}O_6$ octahedra then became distorted (Jahn-Teller distortion). The vertical dotted lines represent the energy levels of Mn^{3+} t_{2g} and e_g orbitals in the absence of the Jahn-Teller effect. The Mn^{3+} e_g orbital (occupied by a single electron) is at a higher energy level than the Mn^{2+}/Co^{2+} t_{2g} orbitals, due to the larger crystal field splitting in octahedral symmetry. As $c/\sqrt{2}a$ (indicator of $Mn^{3+}O_6$ distortion) decreases with an increase in Co content, the octahedral distortion is suppressed (Mn^{3+} e_g orbital splitting becomes smaller) and the single electron occupying the Mn^{3+} e_g orbital shifts to a higher energy level.

In this context, we chose to examine whether the electronic state of Mn^{3+} changes in favor of enhancing the OER activities for $Mn_{3-x}Co_xO_4$ ($0 \leq x < 1$). Since lattice, spin and orbital degrees of freedom are strongly coupled for the Mn^{3+}-based tetragonally distorted spinel species,[29,30,31] the electronic state of Mn^{3+} can be probed by the crystal structure. Therefore, we examined the electronic state of Mn^{3+} focusing on the Jahn-Teller distortion of $Mn^{3+}O_6$ octahedra. When $3d$ transition metals (M) are situated at the center of the MO_6 octahedra, their $3d$ orbitals split into triply degenerated t_{2g} orbitals and doubly degenerated e_g orbitals. As Mn^{3+} has four $3d$ electrons, the Mn^{3+} $3d$ orbitals split into two energy levels to lower the total energy of the Mn^{3+} $3d$ electrons (Fig. 4). When the Jahn-Teller distortion of $Mn^{3+}O_6$ octahedra is suppressed (equivalent to $c/\sqrt{2}a$ decreasing) due to the increase in Co content (Fig. S3), the splitting of the Mn^{3+} e_g orbitals becomes smaller and the electron occupying the Mn^{3+} e_g orbital shifts to a higher energy level (Fig. 4). Thus, the overlap of the antibonding Mn^{3+} e_g orbitals with the O $2p$ orbitals of the oxygen adsorbate becomes stronger. The OER activity of $Mn_{3-x}Co_xO_4$ should therefore be enhanced due to the stronger binding of OER intermediates to the catalytic surface. This prediction was experimentally supported by the linear correlation between the indicator of the Jahn-Teller distortion ($c/\sqrt{2}a$) and the OER activity (Fig. 3(d)). The linear correlation becomes more pronounced when the OER activity is divided by the normalized BET surface area (Fig. S4(d)). We could therefore conclude that a correlation exists between the suppression of the Jahn-Teller distortion and the OER activity. For compounds containing Mn^{3+}, not only the number of e_g electrons but also the Jahn-Teller distortion plays a crucial role in their OER activities. Minimizing the

Jahn-Teller distortion (without changing the number of e_g electrons) could further improve the OER activities of Mn^{3+} based compounds. Since the suppression of the Jahn-Teller distortion (by increasing the Co content) is physically equivalent to raising the temperature of Mn_3O_4 (Mn_3O_4 becomes cubic at 1170 °C[32]), our result suggests a future application of $Mn_{3-x}Co_xO_4$ ($0 \leq x < 1$) as an energy saving catalyst for metal-air batteries.

In contrast, the OER performance of $Mn_{3-x}Co_xO_4$ decreased with an increase in Co content for $1 < x \leq 1.5$ (Fig. 5). Lower specific OER activities (Fig. S5(a)), slightly larger Tafel slopes (Fig. S5(b)), and relatively constant overpotentials (Fig. S5(c)) were observed for $Mn_{3-x}Co_xO_4$ (x= 1.2, 1.5) when compared to $Mn_{2.1}Co_{0.9}O_4$. This OER behavior can be explained in terms of the electrons in the e_g orbital and the Jahn-Teller distortion, as was the case for $Mn_{3-x}Co_xO_4$ ($0 \leq x < 1$). When the Co content increased above $x > 1$, the octahedral site was occupied by a mixture of Mn^{3+}, Co^{3+}, Mn^{4+}, and Co^{2+} ions[17]. This is in contrast with $Mn_{3-x}Co_xO_4$ ($0 \leq x < 1$) where the octahedral site is occupied only by Mn^{3+} (Fig. S2(a)). When the number of electrons in the e_g orbital changes from unity for transition metal ions, they cannot remain as the OER highly active sites. Therefore, the increase of Mn^{4+} ($t_{2g}^3 e_g^0$) and Co^{2+} ($t_{2g}^5 e_g^2$) concentration (at the epical center of the octahedra) with the increase in Co content degrades the OER activity of $Mn_{3-x}Co_xO_4$ ($1 < x \leq 1.5$). On the other hand, the suppression of Jahn-Teller distortion with the increase in Co content (Fig. S3) elevates the OER activity. These two effects compete with each other, and the OER activities of x = 1.2 and 1.5 drop slightly compared with that of x = 0.9. The reduction in Mn^{3+} ($t_{2g}^3 e_g^1$) concentration degrades the OER activity, but the increase of Co^{3+} (OER active site: $t_{2g}^5 e_g^1$ for surface) compensates this effect. It should be noted that maintaining the concentration of cations with a single e_g electron (Mn^{3+} and Co^{3+} at the octahedral site) is essential to improve the OER activity. Therefore, in summary, the OER performance of $Mn_{3-x}Co_xO_4$ ($1 < x \leq 1.5$) does not contradict with the explanation for the OER performance of $Mn_{3-x}Co_xO_4$ ($0 \leq x < 1$), thus strongly supporting a correlation between the suppression of Jahn-Teller distortion and the OER activity of the material.
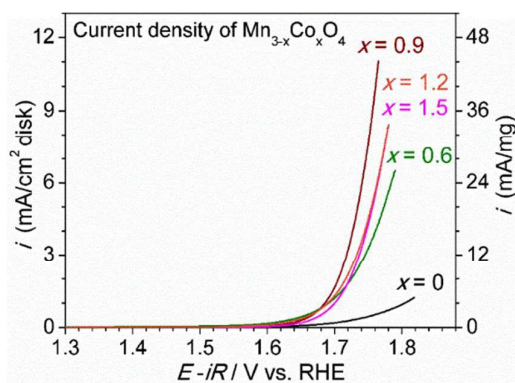
Fig. 5 Linear sweep voltammetry curves of the OER (cycle 10) for $Mn_{3-x}Co_xO_4$ (x = 0, 0.6, 0.9, 1.2, 1.5).

4 Conclusion

We systematically studied the OER performance of $Mn_{3-x}Co_xO_4$ ($0 \leq x < 1$) nanoparticles for the first time. Nanoparticles were prepared at room temperature to minimize the influence of geometric factors. With an increase in Co content, a significant improvement in the OER activity was observed for $Mn_{3-x}Co_xO_4$ ($0 \leq x < 1$). More specifically, $Mn_{2.1}Co_{0.9}O_4$ exhibited a high specific OER activity (1700% of Mn_3O_4 at 1.76 V vs. RHE) and long-term stability over 100 cycles. The OER activities of $Mn_{3-x}Co_xO_4$ ($0 \leq x < 1$) increased linearly with the suppression of the Jahn-Teller distortion. We therefore propose that Jahn-Teller distortion plays an important role in the OER activities of compounds containing Mn^{3+}. The OER performance of Mn^{3+}-based compounds can be further improved by minimizing the Jahn-Teller distortion, suggesting their future application as energy saving catalysts for metal-air batteries. Work is currently ongoing in our group synthesizing Ni^{3+}-based spinel oxides with suppressed Jahn-Teller distortion (using liquid phase synthesis) and exploring their OER performances.

Acknowledgements

References

1. M. Armand and J. M. Tarascon, *Nature*, 2008, **451**, 652.
2. Y. C. Lu, Z. Xu, H. A. Gasteiger, S. Chen, K. Hamas-Schifferli and Y. Shao-Horn, *J. Am. Chem. Soc.*, 2010, **132**, 12170.
3. N. S. Lewis and D. G. Nocera, *Proc. Natl. Acad. Sci. USA*, 2006**, 103**, 15729.
4. M. G. Walter, E. L. Warren, J. R. McKone, S. W. Boettcher, Q. X. Mi, E. A. Santori and N. S. Lewis, *Chem. Rev.*, 2010**, 110**, 6446.
5. Y. Lee, J. Suntivich, K. J. May, E. E. Perry and Y. Shao-Horn, *J. Phys. Chem. Lett.*, 2012, **3**, 399.
6. J. Suntivich, K. J. May, H. A. Gasteiger, J. B. Goodenough and Y. Shao-Horn, *Science*, 2011, **334**, 1383.
7. U. Maitra, B. S. Naidu, A. Govindaraj and C. N. R. Rao, *Proc. Natl. Acad. Sci. USA*, 2013, **110**, 11704.
8. Y. Zhu, W. Zhou, Z. G. Chen, Y. Chen, C. Su, M. O. Tadé and Z. Shao, *Angew. Chem., Int. Ed.*, 2015**, 54**, 3897.
9. J. Kim, X. Yin, K. C. Tsao, S. Fang and H. Fang, *J. Am. Chem. Soc.*, 2014, **136**, 14646.
10. B. Han, M. Risch, Y. L. Lee, C. Ling, H. Lia and Y. Shao-Horn, *Phys. Chem. Chem. Phys.*, 2015, **17**, 22576.
11. V. Baron, J. Gutzmer, H. Rundlof and R. Tellgren, *Am. Mineral.*, 1998, **83**, 786.
12. S. Cimino, S. Colonna, S. De Rossi, M. Faticanti, L. Lisi, I. Pettiti and P. Porta, *J. Catal.*, 2002, **205**, 309.
13. X. Sun and D. Li, *Adv. Mat. Res.*, 2014, **834–836**, 458.
14. G. Z. Aminoff, *Kristallogr.*, 1926, **64**, 475.
15. Y. Xiao, D. E. Wittmer, F. Izumi, S. Mini, T. Graber and P. Viccaro, *J. Appl. Phys. Lett.*, 2004, **85**, 736.
16. A. Ramírez, P. Hillebrand, D. Stellmach, M. M. May, P. Bogdanoff and S. Fiechter, *J. Phys. Chem. C,* 2014, **118**, 14073.

17. H. Bordeneuve, C. Tenailleau, S. Guillemet-Fritsch, R. Smith, E. Suard and A. Rousset, *Solid State Sci.*, 2010, **12**, 379.

18. E. Lee, J. H. Janh and Y. U. Kwon, *J. Power Sources*, 2015, **273**, 735.

19. L. Wang, X. Zhao, Y. Lu, M. Xu, D. Zhang, R. S. Ruoff, K. J. Stevenson and J. B. Goodenough, *J. Electrochem. Soc.*, 2011, **158**, A1379.

20. C. Li, X. Han, F. Cheng, Y. Hu, C. Chen and J. Chen, *Nature Commun.*, 2015, **6**, 1.

21. F. Cheng, J. Shen, B. Peng, Y. Pan, Z. Tao and J. Chen, *Nature Chem.*, 2011, **3**, 79.

22. E. Rios, J. L. Gautier, G. Poillerat and P. Chartier, *Electrochim. Acta*, 1998, **44**, 1491.

23. A. C. Larson and R. B. Von Dreele, *Los Alamos National Laboratory Report LAUR*, 2000, 86.

24. J. Suntivich, H. A. Gasteiger, N. Yabuuchi and Y. Shao-Horn, *J. Electrochem. Soc.*, 2010, **157**, B1263.

25. J. I. Jung, H. Y. Jeong, J. S. Lee, M. G. Kim and J. Cho, *Angew. Chem., Int. Ed.*, 2014, **53**, 4582.

26. J. Tafel, K. Schmitz, K. Naremann and B. Z. Emmert, *Phys. Chem.*, 1905, **50**, 641.

27. G. T. Burstein, *Corros. Sci.*, 2005, **47**, 2858.

28. (Electronic Supplementary Information) $Mn_{3-x}Co_xO_4$ nanoparticles had BET surface areas of 60 m^2/g ($x = 0$), 70 m^2/g ($x = 0.3$), 65 m^2/g ($x = 0.6$), and 74 m^2/g ($x = 0.9$).

29. R. Tackett, G. Lawes, B. C. Melot, M. Grossman, E. S. Toberer and R. Seshadri, *Phys. Rev. B*, 2007, **76**, 024409.

30. T. Suzuki and T. Katsufuji, *Phys. Rev. B*, 2008, **77**, 220402.

31. Y. Nii, H. Sagayama, H. Umetsu, N. Abe, K. Taniguchi and T. Arima, *Phys. Rev. B*, 2013, **87**, 195115.

32. H. F. McMurdie, B. M. Sullivan and F. A. Mauer, *J. Res. Nat. Bur. Stand.*, 1950, **45**, 35.

Table of Contents

The suppression of the Jahn-Teller distortion elevates the oxygen evolution reaction activity for $Mn_{3-x}Co_xO_4$ ($0 \leq x < 1$).